JACS
JOURNAL OF THE AMERICAN CHEMICAL SOCIETY

pubs.acs.org/JACS
Article

Multimodal Nanoscale Mapping of Local Structure and CO_2 Adsorption in Metal–Organic Frameworks

Sarah L. Karstens, Matthew N. Dods, Ambarneil Saha, Máté Garai, William Dai, Katerina I. Graf, Ryan A. Klein, Henry Z. H. Jiang, Jung Cho, Karen C. Bustillo, Markus B. Raschke, Peter Ercius, Jeffrey R. Long,* and Andrew M. Minor*

Cite This: *J. Am. Chem. Soc.* 2026, 148, 8474–8486

Read Online

ACCESS | Metrics & More | Article Recommendations | Supporting Information

ABSTRACT: Diamine functionalization of the metal–organic framework Mg_2(dobpdc) (dobpdc^{4-} = 4,4′-dioxidobiphenyl-3,3′-dicarboxylate) significantly enhances its selectivity for CO_2 capture from flue gases and air. The structure and CO_2 capacity of such materials are typically assessed using bulk techniques that rely on averaging signal over large ensembles of unit cells, obscuring local heterogeneities, such as variations in CO_2 occupancy across individual nanocrystals. To resolve this limitation, we demonstrate a multimodal, nanoscale characterization of Mg_2(dobpdc) appended with 1,3-diaminopropane. By employing recently developed characterization techniques at progressively smaller length scales, we uncover insights from correspondingly smaller populations of unit cells. First, we use parallel-beam 3D electron diffraction (3D ED) to identify a prominent expansion in lattice parameters upon desorption of CO_2, as observed at the level of single nanocrystals. Second, we use convergent-probe 4D scanning transmission electron microscopy (4D-STEM) to quantify associated differences in lattice strain as a function of gas loading and diamine appending. These measurements sample small subvolumes within individual nanocrystals. Finally, we apply infrared scattering scanning near-field optical microscopy (IR *s*-SNOM) to confirm variable CO_2 chemisorption across adsorption sites at the surface of single nanocrystals. This multimodal, multiscale approach allows us to map heterogeneity within individual nanocrystals. Collectively, these findings emphasize the importance of local, nanoscale characterization of metal–organic frameworks in revealing previously unresolvable features that impact their performance.

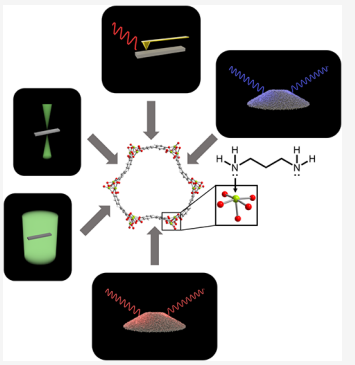

INTRODUCTION

Metal–organic frameworks (MOFs) have attracted interest for a range of applications, including catalysis,[1,2] drug delivery,[3,4] and gas storage and separations.[5−10] For gas storage and separations, these materials enable the tuning of host–guest interactions between the framework and small molecules.[11−13] Currently, host–guest interactions in MOFs are either understood via theoretical simulations or bulk characterization techniques such as gas adsorption isotherms, X-ray or neutron diffraction (XRD/ND), diffuse reflectance infrared spectroscopy (DRIFTS), and nuclear magnetic resonance (NMR) spectroscopy.[14,15] However, these bulk experimental techniques average out information such as spatial heterogeneity among many adsorption sites. Among the highest resolution structural characterization methods for MOFs is single crystal X-ray diffraction (SCXRD), which requires periodicity over multiple micrometers in length.[15−17] In many cases, however, it is difficult to grow sufficiently large single crystals of a MOF, or to maintain such order for *in situ* gas dosing studies, where aperiodic features such as defects and interfaces can affect mass transport properties.[18−22] Recently, Yamada and coworkers reported the visualization of spatially heterogeneous water adsorption inside a 100 μm-scale Co_2(dobdc) (dobdc^{4-} = 2,5-dioxido-1,4-benzenedicarboxylate) crystal using *operando* X-ray absorption fine structure spectroscopy combined with computed tomography.[20]

In contrast to X-ray techniques, which typically have probe sizes on the order of hundreds of micrometers to millimeters, electron microscopy probe sizes range from a few microns to subangstrom level (Figure 1).[23−26] Thus, electron microscopy provides a local probe that can be used to examine a myriad of elusive performance-related aspects of MOFs, including host–guest interactions and structure–property relationships in small crystals, partial loading of a gas within a crystal, and sorption variations between crystals in an ensemble.[12,13,22,27] Transmission electron microscopy (TEM) has only rarely been employed for MOFs due to their sensitivity to electron-beam induced radiolysis, heating, and knock-on damage. Indeed,

Received: November 6, 2025
Revised: February 9, 2026
Accepted: February 11, 2026
Published: February 20, 2026

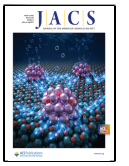

https://doi.org/10.1021/jacs.5c19737
J. Am. Chem. Soc. 2026, 148, 8474–8486

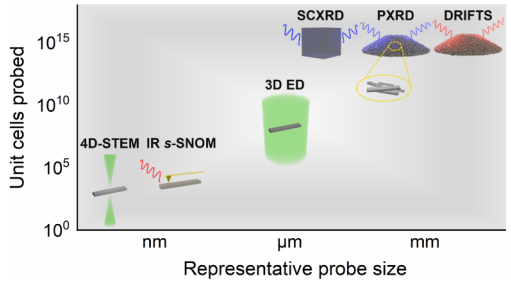

Figure 1. Representative probe size of traditional methods (top right) to examine structure and composition in metal−organic frameworks compared to that of local techniques utilized in this study.

irradiation under typical TEM conditions causes collapse of the structure within seconds.[14,21,25,28−33]

In the past several years, there have been efforts to develop dose-efficient protocols to investigate local structures in MOFs, mainly using high-resolution TEM (HRTEM) and phase contrast scanning transmission electron microscopy (STEM) to directly image the sample, and 3D electron diffraction ("3D ED," "MicroED," "cRED," etc.) to image the reciprocal space.[11,21,22,25,28,31−40] However, to our knowledge there are no previous nanoscale-resolution studies providing dual-space (i.e., real and reciprocal space) visualization of the same MOF.[20] Furthermore, while the methodology has improved, many of the reported electron microscopy studies have been proof-of-concept studies, investigating a select few frameworks that have already been well characterized and are not among the top-performing candidates for a potential application.[41−44]

Here, we will focus instead on investigating performance-related aspects of a framework relevant for CO_2 separation. Diamine-appended variants of Mg_2(dobpdc) (dobpdc^{4-} = 4,4′-dioxidobiphenyl-3,3′-dicarboxylate) are recognized as leading candidates for the capture of CO_2 from flue gases and air.[45−50] The framework Mg_2(dobpdc) provides stability and a high CO_2 removal capacity, which are important for industrial applications, while various diamines can be postsynthetically appended onto the metal sites to improve the selectivity of the framework for CO_2 (Figure 2a).[48,51,52] The specific desired conditions for carbon capture, such as temperature and pressure, can be further tuned based on the selected diamine.[51] Structural characterization via SCXRD conducted on analogous materials, diamine-appended variants of Zn_2(dobpdc), showed that CO_2 adsorption proceeds via a cooperative mechanism whereby the gas molecule inserts into the Zn−N bonds of the framework, forming ammonium carbamate chains (Figure 2b).[46,51] Evidence for this mechanism in diamine-appended Mg_2(dobpdc) is supported by results from ^{13}C NMR, *in situ* DRIFTS, density-functional theory (DFT) simulations, statistical mechanical modeling, and PXRD refinements.[45,53−56] However, attempts at direct structural characterization of the magnesium analog, which is more desirable for CO_2 separation from dilute gas streams, have, until now, been unsuccessful. Specifically, it has not been possible to grow large enough single crystals to characterize Mg_2(dobpdc) and its amine-appended variants with SCXRD.[45,49,50] Furthermore, the CO_2 capacities of these frameworks have only been characterized in bulk via gas adsorption measurements. The occupancies of the chemisorbed gas molecules within individual crystals of the MOF are unknown.

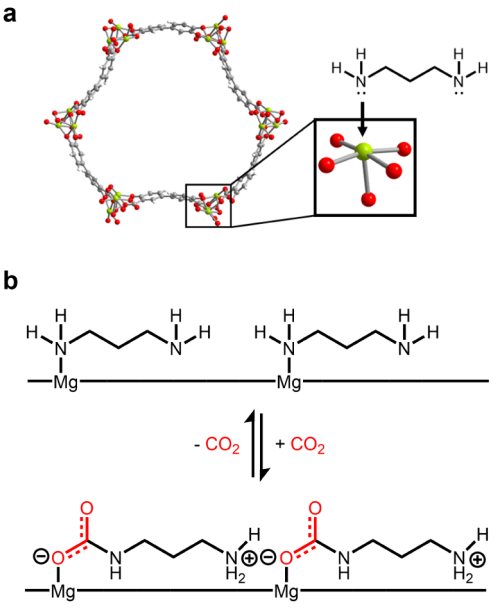

Figure 2. (a) Schematic of diamine appending onto the open metal site of Mg_2(dobpdc) and (b) proposed mechanism of formation of ammonium carbamate chains upon CO_2 exposure.[45,51,53,57] Reproduced from ref 75. Copyright 2024 American Chemical Society.

To answer these longstanding questions, we started by investigating the impact of CO_2 on the structure of the host framework, pn−Mg_2(dobpdc) (pn = 1,3-diaminopropane). We conducted 3D ED on the CO_2-adsorbed MOF, followed by *in situ* heating under vacuum to desorb any CO_2 species in the framework, and then collected 3D ED data of its activated phase. In 3D ED, electron diffraction patterns are recorded at different tilt angles to reconstruct the three-dimensional reciprocal space. Although the setup is analogous to X-ray crystallography, the Coulombic nature of the electron-sample interactions is much stronger than the uncharged X-ray-sample interactions in SCXRD.[58] Thus, 3D ED enables structural solution from smaller single crystals; furthermore, lighter atoms, from which X-rays scatter only weakly, can be more readily resolved.[36,59] The probe in 3D ED is a few micrometers wide, and a postspecimen aperture restricts the detected region to an individual nanocrystal.[60] Besides obtaining an *ab initio* 1.0-Å resolution electrostatic potential map of pn−CO_2−Mg_2(dobpdc)—the first for any variant of Mg_2(dobpdc)[45,50,51]—we uncovered an anisotropic expansion of the unit cell upon CO_2 desorption.

This difference in lattice parameter between CO_2-adsorbed and activated phases was then used to inform 4D scanning transmission electron microscopy (4D-STEM) of pn−Mg_2(dobpdc). In 4D-STEM, a localized electron probe is rastered across the sample and a diffraction pattern is collected at every probe position. Fast detection renders 4D-STEM a dose-efficient technique. Postprocessing of the data (i.e., use of virtual apertures on the diffraction patterns) allows for extraction of real space features resolved on the nanoscale.[24,61] The unique capability of 4D-STEM to enable local, dual-space visualization makes this technique ideal for probing structural heterogeneity in the material. With this method, we were able to connect distributions in lattice parameter value to variations in CO_2 occupancy and amine appending within a single particle.

https://doi.org/10.1021/jacs.5c19737
J. Am. Chem. Soc. 2026, 148, 8474−8486

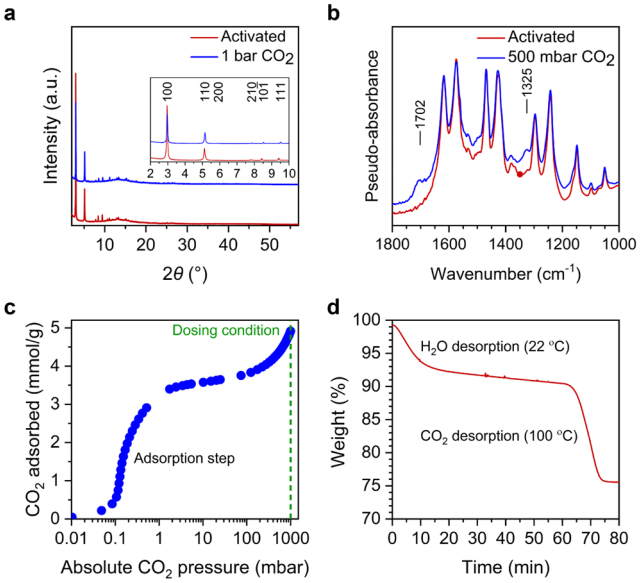

Figure 3. Traditional bulk characterization of pn−Mg_2(dobpdc). (a) Powder X-ray diffraction with *in situ* activation of the CO_2-adsorbed framework. The activation sequence parallels our electron diffraction methodology. (b) *In situ* diffuse reflectance infrared Fourier transform spectra of activated framework upon CO_2 exposure. Lines at 1702 and 1325 cm^{-1} mark the diagnostic ν(C−O) and ν(C−N) bands, respectively, of the carbamate that forms upon CO_2 adsorption. (c) Dry CO_2 isotherm at 25 °C indicating an adsorption step well below the dosing condition of 1 bar used in our microscopy studies. At this plateau, the adsorption capacity is 89% of the theoretical capacity (4.2 mmol/g), corresponding to one CO_2 molecule per Mg site. (d) Thermogravimetric analysis showing desorption of water and weakly bound CO_2 followed by activation (CO_2 desorption) at 100 °C. This sequence simulates the *in situ* activation in the electron microscope, indicating CO_2 should be desorbed after activation.

Complementary infrared scattering scanning near-field optical microscopy (IR *s*-SNOM) measurements were employed to probe the presence of chemisorbed CO_2 inside a single particle of pn−Mg_2(dobpdc) by relating the CO_2-induced chemical modification to changes in the characteristic optical vibrational response. Specifically, the C−N stretch at ∼1328 cm^{-1}, which is attributed to the formation of an ammonium carbamate species, was tracked as a function of position throughout the crystal.[45,51,57] In IR *s*-SNOM, the metallic tip of an atomic force microscope (AFM) serves to localize broadband infrared radiation, and the near-field interactions enable vibrational spectroscopy with nanometer spatial resolution.[62,63] IR *s*-SNOM has a similar spatial resolution to 4D-STEM but is surface sensitive, probing only the top several nanometers of the material. Taken together, our multimodal approach comprising techniques that probe progressively smaller regions of a MOF provides new insights into heterogeneity arising from host−guest interactions and material functionalization.

RESULTS AND DISCUSSION

3D Electron Diffraction

Although the pn−Mg_2(dobpdc) crystals diffracted well (Figures 3a and S6), their submicron size (Figures 4c and S1) precluded SCXRD as a viable method for structural elucidation, rendering the sample a good candidate for 3D ED. Furthermore, both the CO_2-adsorbed phase and the activated phase could be accessed within the working parameters of the TEM.[51] At room temperature under vacuum (i.e., 8×10^{-8} Torr in the TEM column), CO_2 is expected to remain chemisorbed in pn−CO_2−Mg_2(dobpdc). Heating at 100 °C under vacuum for 1 h promotes complete CO_2 desorption, resulting in the activated material pn−Mg_2(dobpdc) (Figure 3d). Accordingly, we collected 3D ED data (using different crystals for each measurement to reduce beam damage effects) before and after *in situ* activation, allowing for a direct comparison of the two phases. To negate the effects of thermal expansion on the structure, we conducted the activated phase measurements at room temperature. Precautions were taken to mitigate beam damage effects. Most notably, no measured crystal was exposed to the beam prior to data collection. This is not standard practice in most TEM experiments, where the crystal is irradiated prior to data collection in order to find and focus the sample.

We compared data sets from three crystals of the CO_2-adsorbed phase with four crystals of the activated phase, all from the same *in situ* session. The material was loaded as pn−CO_2−Mg_2(dobpdc), measured, then heated *in situ* to yield activated pn−Mg_2(dobpdc), which was subsequently measured at room temperature. This sequence was simulated using thermogravimetric analysis (TGA), which measures changes in sample mass as a function of temperature, to confirm activation (Figures 3d and S12). Autoindexing of each individual data set led to the assignment of lattice parameters in agreement with various SCXRD solutions of diamine-appended Zn_2(dobpdc) (Table S1). The determined space group for both phases, $P3_121$, also aligned with solutions of these Zn analogs.[51] As visualized in Figure S2, $a = b$ values ranged from 20.862 ± 0.045 Å to 21.014 ± 0.021 Å for the CO_2-adsorbed phase compared to 21.317 ± 0.002 Å to 21.522 ± 0.007 Å for the activated phase. Table 1 illustrates the average of these results. Upon desorption of CO_2, the material expanded ∼0.5 Å (2.4%) in the $a = b$ direction, commensurate with the face of the pore (Figure 4a) (the longest crystallite direction aligns with the c axis).[64−66] Previous unit cell parameter determinations of diamine-appended Mg_2(dobpdc) via DFT and Pawley fits of PXRD data do not indicate a consistent trend of contraction in the $a = b$ direction upon CO_2 adsorption (Table

Table 1. Lattice Parameters for pn−Mg_2(dobpdc) Derived from 3D ED, PXRD, and DFT (Unit: Å)[a]

	3D electron diffraction[b,c]		Powder X-ray diffraction[b,c]		Density functional theory[d]	
	Activated	CO_2-dosed	Activated	CO_2-dosed	Activated	CO_2-dosed
$a = b$	21.427 ± 0.023	20.925 ± 0.030	21.3958(2)	21.2967(2)	21.544,[67] –	20.688,[67] 21.028[54]
c	6.862 ± 0.040	6.914 ± 0.007	6.9409(2)	6.8485(2)	6.794,[67] –	7.056,[67] 7.051[54]

[a]All structures belong to the trigonal crystal system ($\alpha = \beta = 90°$, $\gamma = 120°$). [b]Crystallography data were collected at room temperature. [c]The method to calculate error and precision in lattice parameter determination is very different in 3D ED and PXRD and therefore should not be compared. [d]Temperature was not reported for the DFT calculations.

https://doi.org/10.1021/jacs.5c19737
J. Am. Chem. Soc. 2026, 148, 8474−8486

S1).[51,52,57] The same is true for structures of diamine-appended Zn_2(dobpdc) solved via SCXRD.[51,57] This lack of a consistent trend across all findings for diamine-appended M_2(dobpdc) (M = Mg, Zn) is unsurprising, because the choice of both metal and amine affect the nature and strength of CO_2 adsorption, in turn affecting the relative stability of the activated and CO_2-adsorbed phases.[51,57]

We suggest, however, that the more pronounced difference in $a = b$ between the two phases compared to literature values comes not only from slight differences in composition, but also from the more local nature of 3D ED compared to SCXRD and PXRD. Considering the morphology observed by (S)TEM (Figure S1), the sample thickness measured by AFM (Figure 6a), and the unit cell volume, we estimate that 10^8 unit cells were averaged to determine the unit cell parameters of each phase using 3D ED data. Given the larger crystal size requirement for SCXRD, the resulting structural solutions derive from an average over 10^{15} unit cells—7 orders of magnitude more than results from 3D ED. Results from PXRD average over similar orders of unit cells as from SCXRD, but across many different crystallites (Figure 1). Defects in crystals can hinder adsorption, and our 3D ED data reveal that adsorption has a measurable effect on the unit cell parameters. If a batch of dosed crystals measured with PXRD comprises a mixture of MOFs with different concentrations of defects, the resulting unit cell parameters will not accurately reflect those of a MOF with complete CO_2 adsorption. Consequently, for any imperfect samples, PXRD may be ill-suited to characterize accurately the structural changes upon guest molecule incorporation, whereas each 3D ED data set is specific to a single crystal. Indeed, through Pawley fits of *in situ* PXRD measurements at 298 K mirroring our 3D ED setup (Figure 3a), we found $a = b$ for the CO_2-adsorbed phase to be 21.2967 ± 0.0002 Å compared to 21.3958 ± 0.0002 Å for the activated phase (Table 1); that is, expansion upon desorption of CO_2 was evident, but to a lesser extent than in our 3D ED measurements. The CO_2 adsorption isotherm conducted on the bulk powder at room temperature (Figure 3c) reinforces the hypothesis that the sample comprises crystals with varying CO_2 capacities. The samples were dosed with 1 bar of dry CO_2 to ensure maximal CO_2 adsorption, but the adsorption step plateaus at a much lower pressure, ∼10 mbar. The theoretical CO_2 capacity of pn−Mg_2(dobpdc) is 4.2 mmol CO_2/g, assuming 1 CO_2 molecule per metal site is adsorbed (Figure 2b). The measured capacity at the adsorption step plateau is 89.4%, or 3.82 mmol CO_2/g pn−Mg_2(dobpdc). It is therefore reasonable to postulate that while the vast majority of the metal sites participate in cooperative formation of ammonium carbamate moieties, some sites do not. This imperfect capacity could arise from defects or pore blockages for example. We cannot deduce from the bulk isotherm how these ill-performing sites are distributed; that is, whether it is a collection of crystals with partial CO_2 occupation, or a mixture of crystals with complete occupation and others with none. The range of $a = b$ values from 3D ED measurements suggest the former, but an even smaller probe is necessary to visualize variability in occupation across a single nanocrystal.

Although the 3D ED-derived unit cell parameters were a result of averaged data sets from the same *in situ* activation session, every individual data set displayed the same trend (the autoindexed $a = b$ values for the CO_2-adsorbed phase were consistently smaller than those of the activated phase) (Figure S2). Higher resolution data collected in a separate session, used to generate an *ab initio* 1.0-Å resolution electrostatic potential map of the CO_2-adsorbed phase, were also autoindexed to reveal smaller $a = b$ parameters compared to all measurements of the activated phase.

The ability to merge intensities from separate crystals, which is a common solution to the hardware limitation of the missing wedge in 3D ED,[68,69] was hindered by the variation in unit cell parameters between different specimens (Figure S2). Furthermore, completeness—the proportion of measured reflections to possible reflections—stayed at 74.9% regardless of the number of merged data sets due to orientation bias on the TEM grid, as the crystals were elongated rectangular plates (Figure 6a). Unambiguous interpretation of weaker features in the obtained electrostatic potential map was therefore not straightforward. As seen in the electrostatic potential map at 3 root-mean-square deviations (σ) (Figure 4a), the MOF was clearly resolved, indicating the long-range order of its rigid scaffold. Additional density within the pore appeared to correspond to features anchored at the metal sites, which could be ammonium carbamate species that propagate as chains along the c axis.[53,54,70] For an assumed 100% CO_2 occupancy, the ammonium carbamates would be clearly resolved at 3σ.[34,36] The fact that they were not suggests partial CO_2 adsorption in the measured crystal.

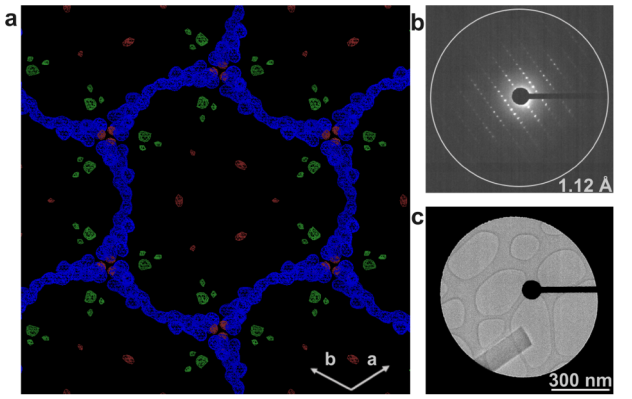

Figure 4. 3D ED of pn−CO_2−Mg_2(dobpdc). (a) Weighted electrostatic potential map ($2F_0$-F_c) contoured at +3σ. The metal nodes and organic ligands that comprise the framework are clearly resolved. Within the pore, additional density attributed to atoms from the ammonium carbamate moieties is visible, but the corresponding atoms are not clearly resolved. (b) Example diffraction pattern from a tilt series and (c) accompanying real space micrograph of the crystal on lacey carbon, taken after the tilt series.

From our 3D ED analysis, we concluded that pn−Mg_2(dobpdc) is isomorphous to many diamine-appended variants of Zn_2(dobpdc), as they share a trigonal space group symmetry and very similar unit cell parameters.[46,51] However, diamine-appended variants of Mg_2(dobpdc) may not be isostructural to their Zn analogs; that is, they may differ in the atomic arrangement of appended amines. Disorder was also present in refinements from SCXRD measurements of Zn_2(dobpdc) and its amine-appended variants.[46,48,51] While 3D ED enabled partial structural elucidation of pn−CO_2−Mg_2(dobpdc), the result was similarly disordered. Heterogeneity, e.g., as a function of partial CO_2 occupancy, was apparent but not completely visualized within a nanocrystal, because parallel-beam TEM still leads to structural solutions that average over ∼10^8 unit cells (Figure 1). A more local

https://doi.org/10.1021/jacs.5c19737
J. Am. Chem. Soc. 2026, 148, 8474−8486

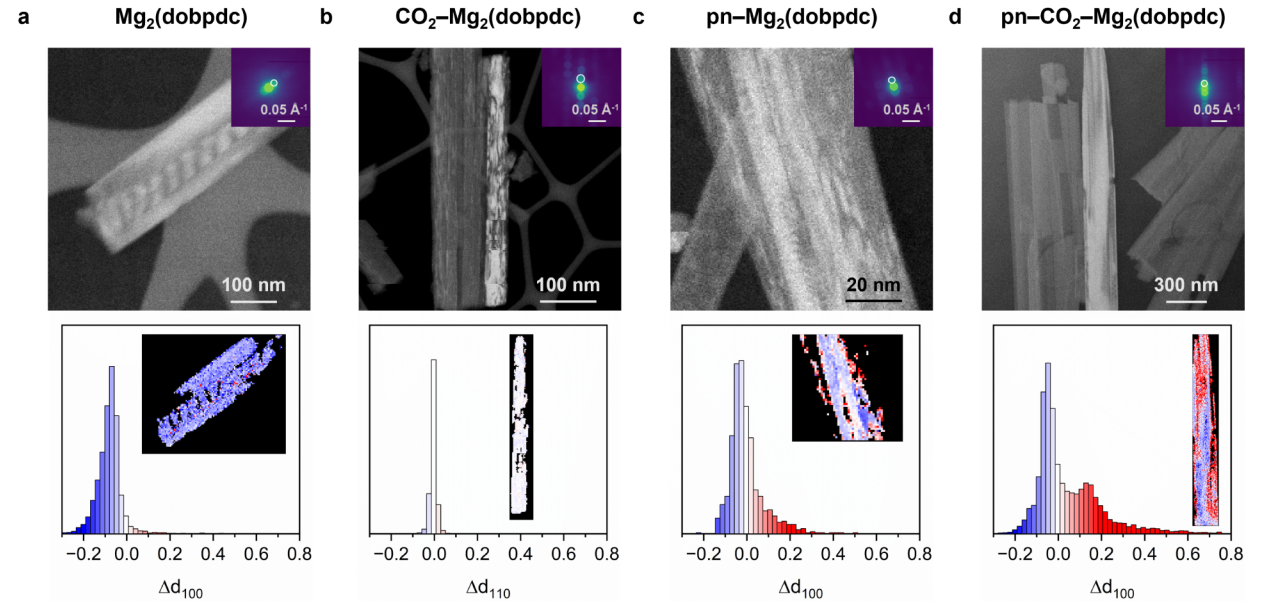

Figure 5. 4D-STEM of variants of Mg_2(dobpdc) crystals. Virtual dark field images (top) highlight diffraction from the selected diffraction plane, circled in white in the inset diffraction pattern. The variation in intensity throughout the crystals reveals their mosaicity, a sign of disorder. Although the selected crystal planes form striations in all cases, the shape and size of these striations are not consistent across the four samples, indicating structural heterogeneity. Lattice parameter maps of these peaks and accompanying histograms are shown at bottom. Strain Δd (± 0.05) was calculated relative to the mean lattice parameter of pn−CO_2−Mg_2(dobpdc) and activated pn−Mg_2(dobpdc), as determined by electron crystallography (d_{100} = 18.36 Å; d_{110} = 10.56 Å). Crystals in (a), (c), and (d) were mapped using d_{100}; however, due to orientational restrictions, (b) was mapped using d_{110}. The results indicate increased structural heterogeneity after the framework is functionalized with diamine (c−d), as well as after the diamine-appended framework is loaded with CO_2 (d).

characterization of structure and disorder in pn−CO_2−Mg_2(dobpdc)—such as that provided by 4D-STEM—was required to fully understand limitations of the 3D ED analysis.

4D-Scanning Transmission Electron Microscopy

Moving from a parallel beam in 3D ED to a convergent one in 4D-STEM reduces the probe size from a micrometer to a few nanometers. Furthermore, while 3D ED is purely a reciprocal space technique, 4D-STEM is a dual-space technique that collects a series of diffraction patterns at many scan points across a sample. Visualization of the crystal structure superimposed on real space is an excellent tool for uncovering structural heterogeneity within a single crystal. Therefore, we used 4D-STEM to map the empirical relationship between gas adsorption and the structural change uncovered by 3D ED.

The 3D ED results showed a measurable change in the $a = b$ unit cell dimension as a function of CO_2 adsorption, so we directed our focus toward 4D-STEM measurements of Mg_2(dobpdc) that included the d_{100} peak. The elongated rectangular morphology of the particles led to orientation bias and few particles with the desired orientation. For additional data, we included data sets with the d_{110} peak, which should still reflect change as a function of CO_2 adsorption but to a smaller degree.

Virtual dark field (VDF) images of these peaks for each sample type (Mg_2(dobpdc), Mg_2(dobpdc) dosed with CO_2, amine-appended Mg_2(dobpdc), and amine-appended Mg_2(dobpdc) dosed with CO_2) are shown in Figure 5. A VDF image uses the collected diffraction patterns to create an image in real space, the contrast of which is dependent on the diffracting condition of the selected lattice plane (in this case, corresponding to the peak d_{100} or d_{110}). High intensity in an area in the VDF image indicates strong diffraction from the selected peak. Inversely, weak diffraction of the crystal plane corresponding to the selected peak manifests in low intensity in the VDF image. A VDF image of a perfect crystal would be uniformly bright or dark, depending on the diffracting conditions. The striations in the VDF images in Figure 5 revealed mosaicity in the crystals, or imperfectly aligned regions of crystallinity consistent with the disorder identified in our 3D ED data. The highlighted features in the VDF images varied in size, shape, and direction, indicating structural heterogeneity not only within a crystal but also between the different samples. To our knowledge, this is the first time these crystalline features in MOFs have been visualized in dual space.

For a more detailed analysis of CO_2 occupation and related heterogeneity within the crystal, we mapped the lattice spacing for the given peak as a function of spatial position. We plotted this lattice spacing with respect to the average of the value expected for activated and CO_2-dosed pn−Mg_2(dobpdc), as calculated from the unit cell parameters and geometry determined from our 3D ED data (Table 1). For example, d_{100} expanded from 18.13 Å in pn−CO_2−Mg_2(dobpdc) to 18.59 Å in activated pn−Mg_2(dobpdc). Thus, our reference value for the d_{100} maps was 18.36 Å. In the case of d_{110}, the expected lattice spacings were 10.72 and 10.47 Å for activated and CO_2-dosed pn−Mg_2(dobpdc), respectively, resulting in a reference value of 10.56 Å for the d_{110} maps. For the sake of comparing distributions of different samples, we used this type of reference for all data sets.

As seen in Figure 5d, the most strained crystal was the diamine-appended, gas-dosed Mg_2(dobpdc), which interestingly displayed a bimodal distribution of d_{100} values. A simple interpretation of this distribution is that it reflects a distinction between gas-filled ($-\Delta d$) and empty regions ($+\Delta d$) of the material. The domain size of these regions ranged from as small as the probe step size (1.56 nm) up to ~600 nm. If this

https://doi.org/10.1021/jacs.5c19737
J. Am. Chem. Soc. 2026, 148, 8474−8486

probed crystal were representative of the bulk powder measured in the isotherm (Figure 3c), we would expect ~90% of the sites to have $-\Delta d$, i.e., a contracted lattice parameter from CO_2 adsorption. Instead, as seen in the histogram in Figure 5d, we observed ~67% of sites with this contracted lattice parameter, despite the excess dosing condition of 1 bar of CO_2. Furthermore, the range of values was larger than expected from the 3D ED findings. This can be explained in part by following the example outlined in the previous section and visualized in Figure 1. Values of d from the 4D-STEM measurement with a 7 nm probe step size represent an average of fewer than 1000 unit cells, 5 orders of magnitude less than the 3D ED data. Thus, the relatively large range of strain values could be attributed to the full distribution of possible values that are provided with the higher spatial resolution sampling of 4D-STEM.

The increasingly local nature of the techniques used in this workflow served to highlight heterogeneity in the MOF crystal. In addition to strain caused by CO_2, there were other sources of strain in the crystals. This is evidenced by the nonsingular distribution of lattice parameter values in activated pn–Mg_2(dobpdc) (Figure 5c). The larger range of lattice parameter values in both of the diamine-appended samples relative to the other two samples of Mg_2(dobpdc) suggests that the process of diamine appending enhances structural heterogeneity of the sample. The material Mg_2(dobpdc) without diamines, whether solvated (Figure 5a) or gas-dosed (Figure 5b), had relatively narrower lattice parameter distributions compared to the diamine-appended counterparts (Figure 5c,d). Since the diamines induce a cooperative adsorption mechanism in diamine-appended M_2(dobpdc) (M = Mg, Mn, Co, Fe, Zn), structural and chemical heterogeneity as a result of incomplete diamine appending could disrupt the propagation of ammonium carbamate chain formation, ultimately affecting the CO_2 adsorption mechanism and crystallinity. Some mosaicity is apparent in all of these samples, and strain could have originated during nucleation and growth of the parent framework Mg_2(dobpdc) for example.

Based on the 4D-STEM results, we propose that Mg_2(dobpdc) exhibits inherent structural heterogeneity, which is exacerbated by diamine appending, and further intensified by CO_2 adsorption. These two processes are invariably linked because incomplete diamine appending would lead to metal sites that cannot participate in the cooperative adsorption mechanism. However, we could not use 4D-STEM to deconvolute the structural effects of diamine appending and CO_2 dosing, since both processes induced strain in the crystals. In this case, chemically specific spectroscopy was needed to probe the CO_2 occupation directly. Therefore, IR *s*-SNOM was employed to map heterogeneity in pn–CO_2–Mg_2(dobpdc) solely as a function of chemisorbed CO_2 occupation.

Infrared Scattering Scanning Near-Field Optical Microscopy

As seen in Figure 3b and in previous studies,[71] peaks at several different wavenumbers in the DRIFTS spectrum appear after dosing pn–Mg_2(dobpdc) with CO_2. Absorption bands at these wavenumbers (1325–1328, 1702, and 3300–3600 cm^{-1}) are considered diagnostic stretches and bends for the formation of an ammonium carbamate species.[45,51,57] Thus, as a proxy for chemisorbed CO_2 (i.e., ammonium carbamate species; see Figure 2b), we tracked the intensity of the C–N stretch at 1328 cm^{-1} as a function of position throughout the crystal, measured in arrays with spatial intervals of 25 nm, as shown in Figure 6b. The C–N *s*-SNOM signal was normalized with respect to the intensity at 1300 cm^{-1}, attributed to bonds in the ligand which do not change upon CO_2 dosing. The relative intensity of the C–N stretch in pn–CO_2–Mg_2(dobpdc) varied with position (Figure 6b), suggesting spatially heterogeneous chemisorption of CO_2. The observed variance in CO_2 adsorption in the crystal supports the 4D-STEM and 3D ED data, indicating that incomplete incorporation of the guest molecules into the framework contributed to structural heterogeneity.

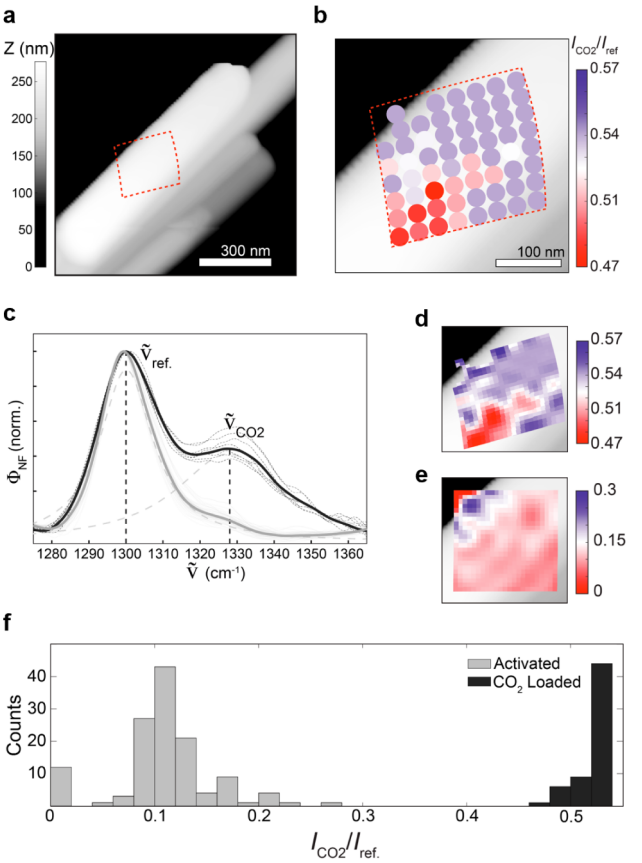

Figure 6. CO_2 loading of pn–Mg_2(dobpdc) mapped by IR *s*-SNOM via the intensity of the C–N stretching vibration at 1328 cm^{-1}, which is associated with the formation of an ammonium carbamate species. (a) AFM topography of a group of nanocrystals. (b) Nano-FTIR array of the outlined area with relative intensity $I(\nu_{CO2})/I(\nu_{ref})$ for each spectrum. (c) Combined spectra revealing the increase and variability (dotted lines) in CO_2 uptake upon loading (dark line; solid lines are Lorentzian fits). Hyperspectral maps of (e) activated pn–Mg_2(dobpdc) showing little to no presence of CO_2, compared to (d) higher but varied amounts in pn–CO_2– Mg_2(dobpdc). (f) Statistical distribution of the referenced peak intensities in the activated and loaded samples.

The variations in CO_2 occupation observed with IR *s*-SNOM were not as extreme as the variations in our 4D-STEM lattice parameter measurements. IR *s*-SNOM is a surface sensitive technique; therefore, CO_2 chemisorption was probed only within the top ~20 nm of the crystal. In contrast, (S)TEM is a transmission technique; the electron beam in 4D-STEM probed the entire thickness of the material, corresponding to an order of magnitude increase in the

https://doi.org/10.1021/jacs.5c19737
J. Am. Chem. Soc. 2026, 148, 8474–8486

number of unit cells sampled in projection. Additionally, it is possible that CO_2 molecules diffuse more slowly to interior adsorption sites compared to surface sites, leading to a disparity in the CO_2 occupancy between the surface and interior of the nanocrystal.[56,72] Although both 4D-STEM and IR *s*-SNOM techniques provide novel information on the nanoscale level, their relative differences purely from their interaction volumes highlight the benefit of our multimodal approach.

CONCLUSION

In this work, we have presented a multimodal nanoscale approach that not only furthers the elucidation of enigmatic crystal structures, but also uncovers and maps heterogeneity in individual MOF crystals. Our observations suggest structural variability in pn–CO_2–Mg_2(dobpdc) is a result of both diamine functionalization and host–guest interactions in the material. We employed 3D ED combined with *in situ* activation to investigate the impact of CO_2 on the host framework. The findings were then used to inform nanoscale mapping of structural features in the MOF via 4D-STEM, while also mapping the chemisorbed CO_2 with IR *s*-SNOM. Broadly, all of these techniques revealed heterogeneity in the material, but each method provided us with unique insights based on their interaction volume.

The 3D ED experiments performed on pn–CO_2–Mg_2(dobpdc) indicated a 0.5 Å expansion in $a = b$ upon desorption of CO_2. Although expansion was sometimes observed in SCXRD studies of diamine-appended variants of the commonly used analog Zn_2(dobpdc), no consistent trend was established.[46,54,73] Our *in situ* PXRD measurements of pn–CO_2–Mg_2(dobpdc) activated to pn–Mg_2(dobpdc) indicated a 0.1 Å expansion in $a = b$ upon CO_2 desorption. Therefore, we suggest the greater extent of structural change in diamine-appended Mg_2(dobpdc) upon CO_2 adsorption compared to other previously reported measurements is connected not only to the difference in the metal, which participates in the CO_2 adsorption mechanism, but also to the reduction of averaging effects obtained with using 3D ED compared to X-ray methods. The crystals showed disorder, as indicated by variations in unit cell parameters and unresolved features attributed to ammonium carbamate species in the electrostatic potential map, resulting in only partial structural elucidation of pn–CO_2–Mg_2(dobpdc).

We sought to further reduce averaging effects and understand the observed disorder using a focused electron probe in 4D-STEM. This approach reduced the probe size from one micrometer to a few nanometers. Measuring lattice spacings corresponding to the $a = b$ plane, we mapped differences in strain in pn–CO_2–Mg_2(dobpdc) and pn–Mg_2(dobpdc), as well as their unfunctionalized variants CO_2–Mg_2(dobpdc) and Mg_2(dobpdc). We found increased distributions of lattice spacings upon diamine functionalization, with the most disparate, bimodal distribution corresponding to amine-appended and CO_2-dosed Mg_2(dobpdc). Although the lattice spacing distributions centered around the expected values from our 3D ED results, the range of values was wider. Corresponding VDF images visualized mosaicity in all of the probed crystals. Based on these results, we conclude that Mg_2(dobpdc) exhibits inherent structural heterogeneity, which is exacerbated by diamine appending, and further by CO_2 adsorption.

Because both diamine appending and CO_2 adsorption impacted local structure in the framework, we sought to isolate local characterization of CO_2 adsorption in pn–CO_2–Mg_2(dobpdc) using spectroscopy. We used IR *s*-SNOM to map CO_2 chemisorption by analyzing the intensity of the C–N stretch at 1328 cm^{-1}, which is only apparent in the CO_2-adsorbed phase. The change in intensity values across the map confirmed variability in CO_2 adsorption within the individual crystal. Unlike our TEM techniques, IR *s*-SNOM offered surface-sensitive chemical characterization of the material.

Altogether, this workflow integrates several techniques not traditionally applied to MOFs to characterize locally a framework of interest in gas storage and separation technologies. We uncovered previously unknown aspects of the material, including an expansion of the pore upon CO_2 desorption, mosaicity, and disorder connected to amine functionalization and incorporation of CO_2. Heterogeneity was observed in CO_2 adsorption using three separate modalities, demonstrating that 3D ED, 4D-STEM, and IR *s*-SNOM are effective tools, complementary to the established bulk techniques, to evaluate and optimize synthetic and postsynthetic modification procedures of MOFs. Overall, we stress the importance of local characterization in these materials to uncover performance-related aspects that are obscured in bulk characterization techniques by averaging effects.

EXPERIMENTAL SECTION

General Procedures

The diamine, metal salt, and solvents were purchased from commercial sources and used as received. The ligand H_4(dobpdc) was purchased from Hangzhou Trylead Chemical Technology and used without further purification. The MOF Mg_2(dobpdc) was prepared according to the literature procedure, as detailed below.[51,54] Laboratory powder X-ray diffraction data were collected on a Bruker AXS D8 Advance diffractometer using Cu Kα radiation (λ = 1.5418 Å) and a zero-background silicon holder.

Synthesis and CO_2 Dosing of pn–Mg_2(dobpdc)[45,51]

A 20 mL scintillation vial was charged with 4 mL of toluene and 1 mL of 1,3-diaminopropane. Methanol-solvated Mg_2(dobpdc) (~50 mg) was filtered and washed with successive aliquots of toluene (2 × 30 mL). Note that Mg_2(dobpdc) should not be allowed to dry completely, as this can in some cases lead to decomposition of the material.[71] Next, Mg_2(dobpdc) was added to the diamine solution, and the vial was swirled several times and allowed to stand at room temperature for 24 h. The mixture was then filtered, and the resulting powder was thoroughly washed with toluene (3 × 20 mL) and allowed to dry for 2 min, yielding ~50 mg of the diamine-appended metal–organic framework. Activation of the samples at 130 °C for 30 min under flowing Ar was sufficient to remove the excess diamine from the pores. A small sample of the product was removed for solution-phase ^{1}H NMR digestion (Figure S13) to assess diamine loading. Approximately 2 mg of material was suspended in 0.5 mL of dimethyl sulfoxide-d_6 and 100 μL of DCl solution (35 g/100 g in D_2O, ≥99 atom % D) was added to dissolve the sample.[74] Data were collected on a Bruker NEO 500 MHz NMR spectrometer and referenced to residual DMSO (δ 2.50 ppm). ^{1}H NMR digestion confirmed that the ratio of diamine to Mg^{2+} sites was ~0.95. The remaining solid was transferred to a glass

https://doi.org/10.1021/jacs.5c19737
J. Am. Chem. Soc. 2026, 148, 8474–8486

adsorption tube equipped with a Micromeritics TransSeal, and activated for an additional 12 h under reduced pressure (<10 μbar) at 100 °C on a Micromeritics 2420 degas manifold. The sample was then transferred air-free to the analysis port of the 2420 adsorption analyzer, dosed with 1 bar of research-grade (>99.998%) CO_2, and allowed to equilibrate for 12 h before removal from the adsorption analyzer.

Gas Adsorption Measurements

The CO_2 adsorption isotherm for pn−Mg_2(dobpdc) was obtained at room temperature by a volumetric method using a Micromeritics 3Flex gas adsorption analyzer and research-grade (>99.995%) CO_2 and N_2. Approximately 112 mg of the framework was loaded into a preweighted sample tube and heated to 100 °C under reduced pressure (<2 μbar) for 12 h in a sand bath. The measurement was carried out at 25 °C. The isotherm data points were considered equilibrated after <0.01% of a pressure change occurred over a 15 s interval.

Thermogravimetric analysis experiments of pn−CO_2−Mg_2(dobpdc) were conducted using a TA Instruments TGA 5500 with a gas flow rate of 25 sccm. Masses were uncorrected for buoyancy effects. The following workflow was carried out to simulate the conditions for 3D ED data acquisition and *in situ* activation in the electron microscope (substituting inert gas as a proxy for vacuum). The sample was subjected to a 100% dry N_2 stream for 1 h to remove weakly bound species such as water. The sample was then activated by heating to 100 °C using a temperature ramp rate of 5 °C/min, and the sample was held isothermally at 100 °C under flowing N_2 for 2 h. To assess whether the previous activation conditions were sufficient, the sample was further heated to 150 °C at a temperature ramp rate of 10 °C/min and held isothermally at 150 °C under flowing N_2 for 10 min, resulting in an additional 1.93% mass loss relative to the starting mass. This additional mass loss, although relatively insignificant, suggests either the volatilization of the amine, which is not stable past 130 °C, or the possibility of a small amount of residual solvent remaining in the pores of pn−Mg_2(dobpdc) after *in situ* activation in the TEM, and could contribute to the distribution of lattice parameters in activated pn−Mg_2(dobpdc) determined by 4D-STEM.

In Situ Diffuse Reflectance Fourier Transform Spectroscopy

[74] DRIFTS data were collected using a Bruker Vertex 70 spectrometer equipped with a glowbar source, KBr beamsplitter, and liquid nitrogen cooled mercury−cadmium−telluride detector. A custom-built diffuse reflectance system with an IR-accessible gas dosing cell was used for all of the measurements. The cell was equipped with a heater controlled by a thermocouple in direct contact with the sample, and the sample atmosphere was controlled by a Micromeritics ASAP 2020Plus gas adsorption analyzer. A sample of the activated framework was dispersed in diamond powder (10 wt %) and evacuated at 100 °C before dosing. Known pressures of CO_2 (99.998%) were dosed into the sample using a Micromeritics ASAP 2020Plus gas sorption analyzer. Spectra at 4 cm^{-1} resolution were generated from 128 scans collected over the course of approximately 35 s and collected at 1 min intervals until no further changes were observed. All spectra were processed in pseudoabsorbance units.

In Situ Powder X-ray Diffraction

A pure, polycrystalline powder of activated pn−Mg_2(dobpdc) was dosed with 1 bar of dry CO_2 for 18 h to generate the carbamate species pn−Mg_2(dobpdc)(CO_2), which was then sealed air-free under N_2. At beamline BL02B2 at SPring-8, the sample (∼10 mg) was packed into a 0.5 mm diameter borosilicate capillary in air (∼5 min), mounted on the goniometer, and connected to the automatic gas handling system at the beamline. The sample was spun at 200 rpm to enhance powder averaging. Scattered X-ray intensity was measured using six one-dimensional solid-state (MYTHEN) detectors.[75] Data were collected with an X-ray energy of 13.0000 keV (i.e., wavelength of 0.95308 Å) with a range of Q from ∼0.2 $Å^{-1}$ to ∼8 $Å^{-1}$. Sample temperature was controlled between 298 and 373 K using a heated nitrogen gas stream flowed over the capillary.[75,76]

The sample was evacuated under dynamic vacuum at 298 K for 30 min (base pressure of 0.1 Pa achieved), with patterns collected every 60 s. A pattern was collected over 360 s representing the room-temperature carbamate material. The sample was then heated at a rate of 10 K/min to 373 K while collecting patterns every 60 s. The sample temperature was held at 373 K for 1 h for activation and to desorb CO_2, with patterns collected every 60 s. Next, a pattern was collected over 360 s at 373 K, and then the sample temperature was decreased at a rate of 2 K/min to 298 K. A pattern was collected over 360 s representing the activated material at 298 K. Pawley fits of the powder patterns at 298 K were used to extract the lattice parameters of CO_2-dosed and activated pn−Mg_2(dobpdc), as detailed in the SI.

3D Electron Diffraction Data Acquisition and Processing

All 3D ED experiments were carried out on an FEI Titan Themis TEM (Thermo Fisher, Eindhoven, The Netherlands) operated at 300 kV. Generally, the workflow for electron diffraction experiments involved the dispersion of a nanocrystalline powder onto a lacey carbon grid and subsequent insertion of the grid into the TEM using an Elsa cryo-transfer holder (Gatan, Pleasanton, USA). A 1.3 μm postspecimen selected area aperture was inserted to isolate the crystal of interest. The crystal was then exposed to parallel illumination and unidirectionally rotated at an angular speed of 2°/s. During this process, a series of diffraction patterns were continuously acquired using 0.25-s exposures throughout the angular wedge sampled. Diffraction patterns were recorded on a Ceta-S CMOS camera. After every series, the beam was blanked and the stage was moved to an unexposed area to avoid irradiation of crystals before data collection.

Data of the CO_2-adsorbed phase were collected at room temperature after waiting >1 h after sample loading into the TEM column; thermogravimetric analysis (Figure 3d) suggested these conditions were largely sufficient to desorb any weakly bound species (such as water). To access the activated phase, the sample was heated at 100 °C in the TEM column and left to equilibrate for >1 h. The heating was then turned off and the sample was left to cool back to room temperature overnight. Data of the *in situ* activated phase were collected at room temperature under the same imaging conditions as the CO_2-adsorbed phase.

Individual diffraction patterns were extracted from each continuous-rotation movie and converted to SMV format using mrc2smv.[77] Indexing, integration, scaling, and merging were conducted using the XDS suite of programs.[78] Integrated

https://doi.org/10.1021/jacs.5c19737
J. Am. Chem. Soc. 2026, 148, 8474−8486

intensities were scaled and merged using XSCALE and then exported to shelx format using XDSCONV. No attempt was made to assign the absolute enantiomorph; the assigned space group ($P3_121$) was arbitrarily selected over its counterpart $P3_221$. A total of seven data sets were utilized for the unit cell determination, comprising three data sets merged for the CO_2-adsorbed and four merged for the activated phase. Separately, an additional pn−CO_2−Mg_2(dobpdc) data set of higher resolution from a different session was processed for structural elucidation. The structure was solved using *ab initio* phasing in SHELXT.[79] In order to produce the electrostatic potential map in Figure 4a, no additional refinement was conducted. Visualization of the electrostatic potential map was done in Coot.[80] Additional details for structural elucidation past the *ab initio* phasing step can be found in the Supporting Information.

4D Scanning Transmission Electron Microscopy and Data Processing

All 4D-STEM experiments were carried out on the double-aberration-corrected TEAM 0.5 instrument, a modified FEI Titan TEM (Thermo Fisher, Eindhoven, The Netherlands) equipped with a Gatan OneView camera and 4D Camera based on the Gatan K3 platform (Gatan, Pleasanton, USA) operating at 87000 fps.[61] A 70 μm condenser aperture was used to produce a beam convergence semiangle of 0.57 mrad (fwhm = 1.78 nm). For pn−CO_2−Mg_2(dobpdc) and Mg_2(dobpdc), a probe step size of 1.56 nm and camera length of 144 and 180 mm, respectively, was used. For pn−Mg_2(dobpdc) and CO_2−Mg_2(dobpdc), a probe step size of 2.24 nm and camera length of 180 mm was used. The probe current was approximately 100 pA.

Data sets were postprocessed using the National Energy Research Scientific Computing Center (NERSC) and visualized using DuSC Explorer, an open-source graphical user interface.[81] Peak detection was carried out in py4DSTEM[82] after the data were binned in real space by 4. The strain in the lattice parameter maps was calculated relative to the mean lattice parameter of the CO_2-adsorbed and activated phases, as determined by 3D ED.

Infrared Scattering Scanning Near-Field Optical Microscopy Acquisition and Data Processing

Microcrystalline pn−CO_2−Mg_2(dobpdc) was thinly deposited onto a clean Si(100) substrate. Isolated single crystals were chosen for further spatio-spectral measurements which were all performed under a purged CO_2 free, 0% RH enclosure. The same crystals were then probed after an ex situ activation step by heating the sample to 100 °C for 16 h in an N_2 purged environment.

IR nanoimaging and spectroscopy were performed using infrared scattering scanning near-field optical microscopy (IR *s*-SNOM) (customized nanoIR2-s prototype, Anasys Instruments/Bruker). A tunable, low-noise, broadband, femtosecond mid-IR laser (Flint, Light Conversion; Levante OPO + HarmoniXX DFG, APE) was focused and scattered off a metallic atomic force microscopy (AFM) tip tapping at 350 kHz (Pt/Ir coated, ARROW-NCPt-50, NANOWorld) as described previously.[62,63] The optical frequency of the generated femtosecond laser pulse was centered around ν_0 = 1320 cm^{-1} (λ = 7.5 μm) with a fwhm bandwidth of 100 cm^{-1} with 3 mW focused onto the tip−sample area. The setup was configured as an asymmetric Michelson interferometer with the sample arm containing the near-field tip−sample interaction and the reference arm with the moving reference mirror. The tip-scattered light was then combined with the reference beam and was detected by a HgCdTe (MCT) detector. The oscillating signal was lock-in demodulated (Zurich Instruments HF2LI) at twice the tip tapping frequency isolating the near-field signal of the material response. By scanning the reference arm, an interferogram of the combined light was detected (nano-FTIR). Each interferogram was collected over a 50 s scan of 1.4 mm distance (corresponding to 3.5 cm^{-1} spectral resolution) of the reference mirror. The interferogram was Fourier transformed into a complex valued frequency response of the material in which the near-field signal is given by $\tilde{E}_{NF}(\upsilon) = Re[\tilde{E}_{NF}(\upsilon)] + Im[\tilde{E}_{NF}(\upsilon)] = |A|_{NF}(\upsilon)e^{i\Phi_{NF}(\upsilon)}$ resulting in amplitude and phase information which is related to the complex dielectric function of the sample.

The phase response $\Phi_{NF}(\upsilon)$ of the averaged frequency domain spectra of the Si substrate background was then subtracted from the sample spectrum. The resulting spectrum of the phase intensity was then normalized with respect to a nearby ligand vibration at ν_{ref} = 1300 cm^{-1} which is invariant under CO_2 adsorption. The normalized spectra were fit using two Lorentzian peaks centered at fixed ν_{ref} = 1300 cm^{-1} and ν_{CO2} = 1328 ± 1 cm^{-1} and fixed width Γ making the peak intensities (Φ_{CO2} and Φ_{ref}) the only free variables. Fits with R^2 < 0.8 were excluded from further processing and plotting as these appeared representative of spectra not taken on the crystal surface but on the substrate, and therefore did not carry any sample information. The fitted ν_{probe} intensities were then mapped onto their respective positions on the high-resolution AFM scan resulting in a spatio-spectral scan of the area. Each point was representative of an ~8^3 nm^3 volume near the crystal surface. Array scans of 8 × 8 points were taken over a 200 × 200 nm area measuring a spectrum in 25 nm intervals.

■ ASSOCIATED CONTENT

Supporting Information

The Supporting Information is available free of charge at https://pubs.acs.org/doi/10.1021/jacs.5c19737.

Additional electron diffraction micrographs and crystallography data, powder diffraction patterns and fits, additional IR *s*-SNOM spectra, TGA trace, and ^{1}H NMR spectrum, relevant electron crystallography data and raw 4D-STEM data (10.5281/zenodo.18111738) (PDF)

■ AUTHOR INFORMATION

Corresponding Authors

Jeffrey R. Long − *Department of Chemistry, University of California, Berkeley, California 94720, United States; Institute for Decarbonization Materials, Department of Chemical and Biomolecular Engineering, and Department of Materials Science and Engineering, University of California, Berkeley, California 94720, United States;* orcid.org/0000-0002-5324-1321; Email: jrlong@berkeley.edu

Andrew M. Minor − *National Center for Electron Microscopy, Molecular Foundry, Lawrence Berkeley National Laboratory, Berkeley, California 94720, United States; Department of Materials Science and Engineering, University of California, Berkeley, California 94720, United States;* orcid.org/0000-0003-3606-8309; Email: aminor@berkeley.edu

https://doi.org/10.1021/jacs.5c19737
J. Am. Chem. Soc. 2026, 148, 8474−8486

Authors

Sarah L. Karstens − *Department of Chemistry, University of California, Berkeley, California 94720, United States; Institute for Decarbonization Materials, University of California, Berkeley, California 94720, United States;* orcid.org/0000-0001-5847-0759

Matthew N. Dods − *Institute for Decarbonization Materials and Department of Chemical and Biomolecular Engineering, University of California, Berkeley, California 94720, United States*

Ambarneil Saha − *National Center for Electron Microscopy, Molecular Foundry, Lawrence Berkeley National Laboratory, Berkeley, California 94720, United States;* orcid.org/0000-0002-6548-5403

Máté Garai − *Department of Physics and JILA, University of Colorado, Boulder, Colorado 80302, United States*

William Dai − *Department of Materials Science and Engineering, University of California, Berkeley, California 94720, United States*

Katerina I. Graf − *Department of Chemistry, University of California, Berkeley, California 94720, United States; Institute for Decarbonization Materials, University of California, Berkeley, California 94720, United States;* orcid.org/0000-0003-3584-7861

Ryan A. Klein − *Department of Chemistry, University of California, Berkeley, California 94720, United States; Institute for Decarbonization Materials, University of California, Berkeley, California 94720, United States; Center for Neutron Research, National Institute of Standards and Technology, Gaithersburg, Maryland 20878, United States;* orcid.org/0000-0002-6807-6701

Henry Z. H. Jiang − *Department of Chemistry, University of California, Berkeley, California 94720, United States; Institute for Decarbonization Materials and Department of Materials Science and Engineering, University of California, Berkeley, California 94720, United States*

Jung Cho − *California NanoSystems Institute, University of California, Los Angeles, California 90095, United States*

Karen C. Bustillo − *National Center for Electron Microscopy, Molecular Foundry, Lawrence Berkeley National Laboratory, Berkeley, California 94720, United States;* orcid.org/0000-0002-2096-6078

Markus B. Raschke − *Department of Physics and JILA, University of Colorado, Boulder, Colorado 80302, United States;* orcid.org/0000-0003-2822-851X

Peter Ercius − *National Center for Electron Microscopy, Molecular Foundry, Lawrence Berkeley National Laboratory, Berkeley, California 94720, United States;* orcid.org/0000-0002-6762-9976

Complete contact information is available at: https://pubs.acs.org/10.1021/jacs.5c19737

Author Contributions

All authors have given approval to the final version of the manuscript.

Funding

U.S. Department of Energy, Office of Science, Basic Energy Sciences, under Contract Nos. DE-SC0019992, DE-AC02−05-CH11231, and BES-ERCAP0032327. National Science Foundation Science and Technology Center under Grant No. DMR-1548924

Notes

The authors declare no competing financial interest.

■ ACKNOWLEDGMENTS

The preparation and bulk characterization of all materials were supported by the U.S. Department of Energy Office of Basic Energy Sciences under award DE-SC0019992. Electron microscopy was supported by the U.S. Department of Energy, Office of Science, Basic Energy Sciences, Materials Sciences and Engineering Division under Contract No. DE-AC02-05-CH11231 within the Electron Microscopy of Soft Matter Program (KC11BN). This work was in part supported by the Laboratory Directed Research and Development Program of Lawrence Berkeley National Laboratory under U.S. Department of Energy Contract No. DE-AC02-05CH11231. IR *s*-SNOM was supported by STROBE: A National Science Foundation Science and Technology Center under Grant No. DMR-1548924. Work at the Molecular Foundry was supported by the Office of Science, Office of Basic Energy Sciences, of the U.S. Department of Energy under Contract No. DE-AC02-05CH1123. The powder synchrotron X-ray diffraction data were performed at BL02B2 in SPring-8 with the approval of the Japan Synchrotron Radiation Institute (JASRI) (Proposal No. 2024B2086). We thank Dr. Yuki Mori (JASRI), Yuto Yabuuchi (UC Berkeley), Isaac Zakaria (UC Berkeley), Dr. Henry Jiang (UC Berkeley), and Katerina Graf (UC Berkeley) for assisting in collecting powder synchrotron X-ray diffraction. We thank Julian Vigil (UC Berkeley) for assistance in collecting and analyzing laboratory powder X-ray diffraction patterns. This research used resources of the National Energy Research Scientific Computing Center (NERSC), a Department of Energy Office of Science User Facility, using NERSC award BES-ERCAP0032327. We thank Drs. Hasan Celik, Raynald Giovine, and the Pines Magnetic Resonance Center's Core NMR Facility (PMRC Core) for spectroscopic assistance. The instruments used in this work were supported by the PMRC Core. We thank Dr. David Prendergast for helpful discussions.

■ REFERENCES

(1) Lee, J.; Farha, O. K.; Roberts, J.; Scheidt, K. A.; Nguyen, S. T.; Hupp, J. T. Metal−Organic Framework Materials as Catalysts. *Chem. Soc. Rev.* **2009**, *38* (5), 1450.

(2) Liao, P.-Q.; Shen, J.-Q.; Zhang, J.-P. Metal−Organic Frameworks for Electrocatalysis. *Coord. Chem. Rev.* **2018**, *373*, 22−48.

(3) Horcajada, P.; Gref, R.; Baati, T.; Allan, P. K.; Maurin, G.; Couvreur, P.; Férey, G.; Morris, R. E.; Serre, C. Metal−Organic Frameworks in Biomedicine. *Chem. Rev.* **2012**, *112* (2), 1232−1268.

(4) Della Rocca, J.; Liu, D.; Lin, W. Nanoscale Metal−Organic Frameworks for Biomedical Imaging and Drug Delivery. *Acc. Chem. Res.* **2011**, *44* (10), 957−968.

(5) Eddaoudi, M.; Kim, J.; Rosi, N.; Vodak, D.; Wachter, J.; O'Keeffe, M.; Yaghi, O. M. Systematic Design of Pore Size and Functionality in Isoreticular MOFs and Their Application in Methane Storage. *Science* **2002**, *295* (5554), 469−472.

(6) Rosi, N. L.; Eckert, J.; Eddaoudi, M.; Vodak, D. T.; Kim, J.; O'Keeffe, M.; Yaghi, O. M. Hydrogen Storage in Microporous Metal-Organic Frameworks. *Science* **2003**, *300* (5622), 1127−1129.

(7) Sumida, K.; Rogow, D. L.; Mason, J. A.; McDonald, T. M.; Bloch, E. D.; Herm, Z. R.; Bae, T.-H.; Long, J. R. Carbon Dioxide Capture in Metal−Organic Frameworks. *Chem. Rev.* **2012**, *112* (2), 724−781.

(8) Han, X.; Yang, S.; Schröder, M. Porous Metal−Organic Frameworks as Emerging Sorbents for Clean Air. *Nat. Rev. Chem* **2019**, *3* (2), 108−118.

(9) Li, J.-R.; Kuppler, R. J.; Zhou, H.-C. Selective Gas Adsorption and Separation in Metal−Organic Frameworks. *Chem. Soc. Rev.* **2009**, *38* (5), 1477.
(10) Gao, M.; Song, B.; Sensharma, D.; Zaworotko, M. J. Crystal Engineering of Porous Coordination Networks for C3 Hydrocarbon Separation. *SmartMat* **2021**, *2* (1), 38−55.
(11) Li, Y.; Wang, K.; Zhou, W.; Li, Y.; Vila, R.; Huang, W.; Wang, H.; Chen, G.; Wu, G.-H.; Tsao, Y.; Wang, H.; Sinclair, R.; Chiu, W.; Cui, Y. Cryo-EM Structures of Atomic Surfaces and Host-Guest Chemistry in Metal-Organic Frameworks. *Matter* **2019**, *1* (2), 428−438.
(12) Chen, Y.; Lu, W.; Schröder, M.; Yang, S. Analysis and Refinement of Host−Guest Interactions in Metal−Organic Frameworks. *Acc. Chem. Res.* **2023**, *56* (19), 2569−2581.
(13) Cho, H. S.; Tanaka, H.; Miyasaka, K.; Terasaki, O. How to Directly Observe and Understand Adsorption: Gas Adsorption Crystallography. *Acc. Mater. Res.* **2023**, *4* (8), 668−680.
(14) Gong, X.; Gnanasekaran, K.; Chen, Z.; Robison, L.; Wasson, M. C.; Bentz, K. C.; Cohen, S. M.; Farha, O. K.; Gianneschi, N. C. Insights into the Structure and Dynamics of Metal−Organic Frameworks via Transmission Electron Microscopy. *J. Am. Chem. Soc.* **2020**, *142* (41), 17224−17235.
(15) Howarth, A. J.; Peters, A. W.; Vermeulen, N. A.; Wang, T. C.; Hupp, J. T.; Farha, O. K. Best Practices for the Synthesis, Activation, and Characterization of Metal−Organic Frameworks. *Chem. Mater.* **2017**, *29* (1), 26−39.
(16) Huang, Z.; Willhammar, T.; Zou, X. Three-Dimensional Electron Diffraction for Porous Crystalline Materials: Structural Determination and Beyond. *Chem. Sci.* **2021**, *12* (4), 1206−1219.
(17) Huang, Z.; Grape, E. S.; Li, J.; Inge, A. K.; Zou, X. 3D Electron Diffraction as an Important Technique for Structure Elucidation of Metal-Organic Frameworks and Covalent Organic Frameworks. *Coord. Chem. Rev.* **2021**, *427*, 213583.
(18) Huang, Z.; Ge, M.; Carraro, F.; Doonan, C.; Falcaro, P.; Zou, X. C. 3D Electron Diffraction Provide Accurate Atomic Structures of Metal−Organic Frameworks? *Faraday Discuss.* **2021**, *225*, 118−132.
(19) Wolff, A. M.; Young, I. D.; Sierra, R. G.; Brewster, A. S.; Martynowycz, M. W.; Nango, E.; Sugahara, M.; Nakane, T.; Ito, K.; Aquila, A.; Bhowmick, A.; Biel, J. T.; Carbajo, S.; Cohen, A. E.; Cortez, S.; Gonzalez, A.; Hino, T.; Im, D.; Koralek, J. D.; Kubo, M.; Lazarou, T. S.; Nomura, T.; Owada, S.; Samelson, A. J.; Tanaka, T.; Tanaka, R.; Thompson, E. M.; Van Den Bedem, H.; Woldeyes, R. A.; Yumoto, F.; Zhao, W.; Tono, K.; Boutet, S.; Iwata, S.; Gonen, T.; Sauter, N. K.; Fraser, J. S.; Thompson, M. C. Comparing Serial X-Ray Crystallography and Microcrystal Electron Diffraction (MicroED) as Methods for Routine Structure Determination from Small Macromolecular Crystals. *IUCrJ* **2020**, *7* (2), 306−323.
(20) Yamada, E.; Sakamoto, H.; Matsui, H.; Uruga, T.; Sugimoto, K.; Ha, M.-Q.; Dam, H.-C.; Matsuda, R.; Tada, M. Three-Dimensional Visualization of Adsorption Distribution in a Single Crystalline Particle of a Metal−Organic Framework. *J. Am. Chem. Soc.* **2024**, *146* (13), 9181−9190.
(21) Zhu, Y.; Ciston, J.; Zheng, B.; Miao, X.; Czarnik, C.; Pan, Y.; Sougrat, R.; Lai, Z.; Hsiung, C.-E.; Yao, K.; Pinnau, I.; Pan, M.; Han, Y. Unravelling Surface and Interfacial Structures of a Metal−Organic Framework by Transmission Electron Microscopy. *Nat. Mater.* **2017**, *16* (5), 532−536.
(22) Liu, Y.; Liu, D.; Liu, Z.; Mao, M.; Zhang, D.; Tao, J.; Zhang, H.; Song, K.; Liu, L.; Han, Y. Electron Microscopy Reveals Inhomogeneous Adsorption of Iodine and Concurrent Defect Formation in a Metal−Organic Framework. *J. Am. Chem. Soc.* **2025**, *147* (5), 3959−3966.
(23) Fewster, P. Characterization of Semiconductors by X-Ray Diffraction and Topography. In *Comprehensive Semiconductor Science and Technology*, 2011; Elsevier Science: Amsterdam; pp. 359−387.
(24) Bustillo, K. C.; Zeltmann, S. E.; Chen, M.; Donohue, J.; Ciston, J.; Ophus, C.; Minor, A. M. 4D-STEM of Beam-Sensitive Materials. *Acc. Chem. Res.* **2021**, *54* (11), 2543−2551.
(25) Li, X.; Wang, J.; Liu, X.; Liu, L.; Cha, D.; Zheng, X.; Yousef, A. A.; Song, K.; Zhu, Y.; Zhang, D.; Han, Y. Direct Imaging of Tunable Crystal Surface Structures of MOF MIL-101 Using High-Resolution Electron Microscopy. *J. Am. Chem. Soc.* **2019**, *141* (30), 12021−12028.
(26) Cusack, S.; Belrhali, H.; Bram, A.; Burghammer, M.; Perrakis, A.; Riekel, C. Small Is Beautiful: Protein Micro-Crystallography. *Nat. Struct. Biol.* **1998**, *5* (8), 634−637.
(27) Ge, M.; Yang, T.; Xu, H.; Zou, X.; Huang, Z. Direct Location of Organic Molecules in Framework Materials by Three-Dimensional Electron Diffraction. *J. Am. Chem. Soc.* **2022**, *144* (33), 15165−15174.
(28) Liu, L.; Zhang, D.; Zhu, Y.; Han, Y. Bulk and Local Structures of Metal−Organic Frameworks Unravelled by High-Resolution Electron Microscopy. *Commun. Chem.* **2020**, *3* (1), 99.
(29) Parent, L. R.; Pham, C. H.; Patterson, J. P.; Denny, M. S.; Cohen, S. M.; Gianneschi, N. C.; Paesani, F. Pore Breathing of Metal−Organic Frameworks by Environmental Transmission Electron Microscopy. *J. Am. Chem. Soc.* **2017**, *139* (40), 13973−13976.
(30) Wiktor, C.; Turner, S.; Zacher, D.; Fischer, R. A.; Tendeloo, G. V. Imaging of Intact MOF-5 Nanocrystals by Advanced TEM at Liquid Nitrogen Temperature. *Microporous Mesoporous Mater.* **2012**, *162*, 131−135.
(31) Zhang, D.; Zhu, Y.; Liu, L.; Ying, X.; Hsiung, C.-E.; Sougrat, R.; Li, K.; Han, Y. Atomic-Resolution Transmission Electron Microscopy of Electron Beam−Sensitive Crystalline Materials. *Science* **2018**, *359* (6376), 675−679.
(32) Gong, X.; Noh, H.; Gianneschi, N. C.; Farha, O. K. Interrogating Kinetic versus Thermodynamic Topologies of Metal−Organic Frameworks via Combined Transmission Electron Microscopy and X-Ray Diffraction Analysis. *J. Am. Chem. Soc.* **2019**, *141* (15), 6146−6151.
(33) Lyu, J.; Gong, X.; Lee, S.-J.; Gnanasekaran, K.; Zhang, X.; Wasson, M. C.; Wang, X.; Bai, P.; Guo, X.; Gianneschi, N. C.; Farha, O. K. Phase Transitions in Metal−Organic Frameworks Directly Monitored through In Situ Variable Temperature Liquid-Cell Transmission Electron Microscopy and In Situ X-Ray Diffraction. *J. Am. Chem. Soc.* **2020**, *142* (10), 4609−4615.
(34) Samperisi, L.; Jaworski, A.; Kaur, G.; Lillerud, K. P.; Zou, X.; Huang, Z. Probing Molecular Motions in Metal−Organic Frameworks by Three-Dimensional Electron Diffraction. *J. Am. Chem. Soc.* **2021**, *143* (43), 17947−17952.
(35) Tien, E.-P.; Cao, G.; Chen, Y.; Clark, N.; Tillotson, E.; Ngo, D.-T.; Carter, J. H.; Thompson, S. P.; Tang, C. C.; Allen, C. S.; Yang, S.; Schröder, M.; Haigh, S. J. Electron Beam and Thermal Stabilities of MFM-300(M) Metal−Organic Frameworks. *J. Mater. Chem. A* **2024**, *12* (36), 24165−24174.
(36) Quintelier, M.; Hajizadeh, A.; Zintler, A.; Gonçalves, B. F.; Fernández De Luis, R.; Esrafili Dizaji, L.; Vande Velde, C. M. L.; Wuttke, S.; Hadermann, J. *In Situ* Study of the Activation Process of MOF-74 Using Three-Dimensional Electron Diffraction. *Chem. Mater.* **2024**, *36* (15), 7274−7282.
(37) Deng, H.; Grunder, S.; Cordova, K. E.; Valente, C.; Furukawa, H.; Hmadeh, M.; Gándara, F.; Whalley, A. C.; Liu, Z.; Asahina, S.; Kazumori, H.; O'Keeffe, M.; Terasaki, O.; Stoddart, J. F.; Yaghi, O. M. Large-Pore Apertures in a Series of Metal-Organic Frameworks. *Science* **2012**, *336* (6084), 1018−1023.
(38) Wang, L.; Ma, M.; Wang, H.; Xiong, H.; Chen, X.; Wei, F.; Shen, B. Real-Space Imaging of the Molecular Changes in Metal−Organic Frameworks under Electron Irradiation. *ACS Nano* **2023**, *17* (5), 4740−4747.
(39) Wang, B.; Rhauderwiek, T.; Inge, A. K.; Xu, H.; Yang, T.; Huang, Z.; Stock, N.; Zou, X. A Porous Cobalt Tetraphosphonate Metal−Organic Framework: Accurate Structure and Guest Molecule Location Determined by Continuous-Rotation Electron Diffraction. *Chem. − Eur. J.* **2018**, *24* (66), 17429−17433.
(40) Ge, M.; Yang, T.; Wang, Y.; Carraro, F.; Liang, W.; Doonan, C.; Falcaro, P.; Zheng, H.; Zou, X.; Huang, Z. On the Completeness of Three-Dimensional Electron Diffraction Data for Structural Analysis of Metal−Organic Frameworks. *Faraday Discuss.* **2021**, *231*, 66−80.

https://doi.org/10.1021/jacs.5c19737
J. Am. Chem. Soc. 2026, 148, 8474−8486

(41) Ye, Z.-M.; Xie, Y.; Kirlikovali, K. O.; Xiang, S.; Farha, O. K.; Chen, B. Architecting Metal−Organic Frameworks at Molecular Level toward Direct Air Capture. *J. Am. Chem. Soc.* **2025**, *147* (7), 5495−5514.
(42) Peng, P.; Jiang, H. Z. H.; Collins, S.; Furukawa, H.; Long, J. R.; Breunig, H. Long Duration Energy Storage Using Hydrogen in Metal−Organic Frameworks: Opportunities and Challenges. *ACS Energy Lett.* **2024**, *9* (6), 2727−2735.
(43) Peng, P.; Anastasopoulou, A.; Brooks, K.; Furukawa, H.; Bowden, M. E.; Long, J. R.; Autrey, T.; Breunig, H. Cost and Potential of Metal−Organic Frameworks for Hydrogen Back-up Power Supply. *Nat. Energy* **2022**, *7* (5), 448−458.
(44) Anastasopoulou, A.; Furukawa, H.; Barnett, B. R.; Jiang, H. Z. H.; Long, J. R.; Breunig, H. M. Technoeconomic Analysis of Metal−Organic Frameworks for Bulk Hydrogen Transportation. *Energy Environ. Sci.* **2021**, *14* (3), 1083−1094.
(45) Milner, P. J.; Siegelman, R. L.; Forse, A. C.; Gonzalez, M. I.; Runčevski, T.; Martell, J. D.; Reimer, J. A.; Long, J. R. A Diaminopropane-Appended Metal−Organic Framework Enabling Efficient CO_2 Capture from Coal Flue Gas via a Mixed Adsorption Mechanism. *J. Am. Chem. Soc.* **2017**, *139* (38), 13541−13553.
(46) Siegelman, R. L.; Milner, P. J.; Forse, A. C.; Lee, J.-H.; Colwell, K. A.; Neaton, J. B.; Reimer, J. A.; Weston, S. C.; Long, J. R. Water Enables Efficient CO_2 Capture from Natural Gas Flue Emissions in an Oxidation-Resistant Diamine-Appended Metal−Organic Framework. *J. Am. Chem. Soc.* **2019**, *141* (33), 13171−13186.
(47) Kim, E. J.; Siegelman, R. L.; Jiang, H. Z. H.; Forse, A. C.; Lee, J.-H.; Martell, J. D.; Milner, P. J.; Falkowski, J. M.; Neaton, J. B.; Reimer, J. A.; Weston, S. C.; Long, J. R. Cooperative Carbon Capture and Steam Regeneration with Tetraamine-Appended Metal−Organic Frameworks. *Science* **2020**, *369* (6502), 392−396.
(48) McDonald, T. M.; Lee, W. R.; Mason, J. A.; Wiers, B. M.; Hong, C. S.; Long, J. R. Capture of Carbon Dioxide from Air and Flue Gas in the Alkylamine-Appended Metal−Organic Framework Mmen-Mg_2 (Dobpdc). *J. Am. Chem. Soc.* **2012**, *134* (16), 7056−7065.
(49) Song, M.; Rim, G.; Mirzazadeh, G.; Hoffman, J.; Moon, H. J.; Leisen, J. E.; Nik, O. G.; Lively, R. P.; Jones, C. W. Amine-Dependent CO_2 Sorption on Amine-Impregnated Mg_2 (Dobpdc) MOF under Humid Conditions. *Ind. Chem. Mater.* **2026**, *4*, 52−64.
(50) Dods, M. N.; Weston, S. C.; Long, J. R. Prospects for Simultaneously Capturing Carbon Dioxide and Harvesting Water from Air. *Adv. Mater.* **2022**, *34* (38), 2204277.
(51) Siegelman, R. L.; McDonald, T. M.; Gonzalez, M. I.; Martell, J. D.; Milner, P. J.; Mason, J. A.; Berger, A. H.; Bhown, A. S.; Long, J. R. Controlling Cooperative CO_2 Adsorption in Diamine-Appended Mg_2 (Dobpdc) Metal−Organic Frameworks. *J. Am. Chem. Soc.* **2017**, *139* (30), 10526−10538.
(52) Lee, J.-H.; Siegelman, R. L.; Maserati, L.; Rangel, T.; Helms, B. A.; Long, J. R.; Neaton, J. B. Enhancement of CO_2 Binding and Mechanical Properties upon Diamine Functionalization of M_2 (Dobpdc) Metal−Organic Frameworks. *Chem. Sci.* **2018**, *9* (23), 5197−5206.
(53) Martell, J. D.; Milner, P. J.; Siegelman, R. L.; Long, J. R. Kinetics of Cooperative CO_2 Adsorption in Diamine-Appended Variants of the Metal−Organic Framework Mg_2 (Dobpdc). *Chem. Sci.* **2020**, *11* (25), 6457−6471.
(54) Forse, A. C.; Milner, P. J.; Lee, J.-H.; Redfearn, H. N.; Oktawiec, J.; Siegelman, R. L.; Martell, J. D.; Dinakar, B.; Zasada, L. B.; Gonzalez, M. I.; Neaton, J. B.; Long, J. R.; Reimer, J. A. Elucidating CO_2 Chemisorption in Diamine-Appended Metal−Organic Frameworks. *J. Am. Chem. Soc.* **2018**, *140* (51), 18016−18031.
(55) Edison, J. R.; Siegelman, R. L.; Preisler, Z.; Kundu, J.; Long, J. R.; Whitelam, S. Hysteresis Curves Reveal the Microscopic Origin of Cooperative CO$_2$ Adsorption in Diamine-Appended Metal-Organic Frameworks. *J. Chem. Phys.* **2021**, *154* (21), 214704.
(56) Kundu, J.; Stilck, J. F.; Lee, J.-H.; Neaton, J. B.; Prendergast, D.; Whitelam, S. Cooperative Gas Adsorption without a Phase Transition in Metal-Organic Frameworks. *Phys. Rev. Lett.* **2018**, *121* (1), 015701.
(57) McDonald, T. M.; Mason, J. A.; Kong, X.; Bloch, E. D.; Gygi, D.; Dani, A.; Crocellà, V.; Giordanino, F.; Odoh, S. O.; Drisdell, W. S.; Vlaisavljevich, B.; Dzubak, A. L.; Poloni, R.; Schnell, S. K.; Planas, N.; Lee, K.; Pascal, T.; Wan, L. F.; Prendergast, D.; Neaton, J. B.; Smit, B.; Kortright, J. B.; Gagliardi, L.; Bordiga, S.; Reimer, J. A.; Long, J. R. Cooperative Insertion of CO2 in Diamine-Appended Metal-Organic Frameworks. *Nature* **2015**, *519* (7543), 303−308.
(58) Gemmi, M.; Mugnaioli, E.; Gorelik, T. E.; Kolb, U.; Palatinus, L.; Boullay, P.; Hovmöller, S.; Abrahams, J. P. 3D Electron Diffraction: The Nanocrystallography Revolution. *ACS Cent. Sci.* **2019**, *5* (8), 1315−1329.
(59) Saha, A.; Nia, S. S.; Rodríguez, J. A. Electron Diffraction of 3D Molecular Crystals. *Chem. Rev.* **2022**, *122* (17), 13883−13914.
(60) Yang, T.; Willhammar, T.; Xu, H.; Zou, X.; Huang, Z. Single-Crystal Structure Determination of Nanosized Metal−Organic Frameworks by Three-Dimensional Electron Diffraction. *Nat. Protoc.* **2022**, *17* (10), 2389−2413.
(61) Ercius, P.; Johnson, I. J.; Pelz, P.; Savitzky, B. H.; Hughes, L.; Brown, H. G.; Zeltmann, S. E.; Hsu, S.-L.; Pedroso, C. C. S.; Cohen, B. E.; Ramesh, R.; Paul, D.; Joseph, J. M.; Stezelberger, T.; Czarnik, C.; Lent, M.; Fong, E.; Ciston, J.; Scott, M. C.; Ophus, C.; Minor, A. M.; Denes, P. The 4D Camera: An 87 kHz Direct Electron Detector for Scanning/Transmission Electron Microscopy. *Microsc. Microanal.* **2024**, *30* (5), 903−912.
(62) Nishida, J.; Alfaifi, A. H.; Gray, T. P.; Shaheen, S. E.; Raschke, M. B. Heterogeneous Cation−Lattice Interaction and Dynamics in Triple-Cation Perovskites Revealed by Infrared Vibrational Nanoscopy. *ACS Energy Lett.* **2020**, *5* (5), 1636−1643.
(63) Muller, E. A.; Pollard, B.; Raschke, M. B. Infrared Chemical Nano-Imaging: Accessing Structure, Coupling, and Dynamics on Molecular Length Scales. *J. Phys. Chem. Lett.* **2015**, *6* (7), 1275−1284.
(64) Colwell, K. A.; Jackson, M. N.; Torres-Gavosto, R. M.; Jawahery, S.; Vlaisavljevich, B.; Falkowski, J. M.; Smit, B.; Weston, S. C.; Long, J. R. Buffered Coordination Modulation as a Means of Controlling Crystal Morphology and Molecular Diffusion in an Anisotropic Metal−Organic Framework. *J. Am. Chem. Soc.* **2021**, *143* (13), 5044−5052.
(65) () Weston, S. C.; Long, J. R.; Falkowski, J. M.; Colwell, K.; Torres, R. Metal-Organic Framework Phase and Crystallite Shape Control WO 2,020,068,996 A1 (accessed 08 July 2025).
(66) Queen, W. L.; Hudson, M. R.; Bloch, E. D.; Mason, J. A.; Gonzalez, M. I.; Lee, J. S.; Gygi, D.; Howe, J. D.; Lee, K.; Darwish, T. A.; James, M.; Peterson, V. K.; Teat, S. J.; Smit, B.; Neaton, J. B.; Long, J. R.; Brown, C. M. Comprehensive Study of Carbon Dioxide Adsorption in the Metal−Organic Frameworks M_2(Dobdc) (M = Mg, Mn, Fe, Co, Ni, Cu, Zn). *Chem. Sci.* **2014**, *5* (12), 4569−4581.
(67) Lee, J.-H.; Hyldgaard, P.; Neaton, J. B. An Assessment of Density Functionals for Predicting CO2 Adsorption in Diamine-Functionalized Metal−Organic Frameworks. *J. Chem. Phys.* **2022**, *156* (15), 154113.
(68) Nannenga, B. L.; Gonen, T. Protein Structure Determination by MicroED. *Curr. Opin. Struct. Biol.* **2014**, *27*, 24−31.
(69) Nannenga, B. L. MicroED Methodology and Development. *Struct. Dyn.* **2020**, *7* (1), 014304.
(70) Vlaisavljevich, B.; Odoh, S. O.; Schnell, S. K.; Dzubak, A. L.; Lee, K.; Planas, N.; Neaton, J. B.; Gagliardi, L.; Smit, B. CO_2 Induced Phase Transitions in Diamine-Appended Metal−Organic Frameworks. *Chem. Sci.* **2015**, *6* (9), 5177−5185.
(71) Milner, P. J.; Martell, J. D.; Siegelman, R. L.; Gygi, D.; Weston, S. C.; Long, J. R. Overcoming Double-Step CO_2 Adsorption and Minimizing Water Co-Adsorption in Bulky Diamine-Appended Variants of Mg_2 (Dobpdc). *Chem. Sci.* **2018**, *9* (1), 160−174.
(72) Kundu, J.; Pascal, T.; Prendergast, D.; Whitelam, S. Selective Gas Capture via Kinetic Trapping. *Phys. Chem. Chem. Phys.* **2016**, *18* (31), 21760−21766.
(73) Siegelman, R. L.; Thompson, J. A.; Mason, J. A.; McDonald, T. M.; Long, J. R. A Cooperative Adsorbent for the Switch-like Capture of Carbon Dioxide from Crude Natural Gas. *Chem. Sci.* **2022**, *13* (40), 11772−11784.

https://doi.org/10.1021/jacs.5c19737
J. Am. Chem. Soc. 2026, 148, 8474−8486

(74) Zhu, Z.; Tsai, H.; Parker, S. T.; Lee, J.-H.; Yabuuchi, Y.; Jiang, H. Z. H.; Wang, Y.; Xiong, S.; Forse, A. C.; Dinakar, B.; Huang, A.; Dun, C.; Milner, P. J.; Smith, A.; Guimarães Martins, P.; Meihaus, K. R.; Urban, J. J.; Reimer, J. A.; Neaton, J. B.; Long, J. R. H.-C. Cooperative CO_2 Capture in a Diamine-Appended Metal−Organic Framework through a Combined Chemisorptive and Physisorptive Mechanism. *J. Am. Chem. Soc.* **2024**, *146* (9), 6072−6083.
(75) Kawaguchi, S.; Takemoto, M.; Osaka, K.; Nishibori, E.; Moriyoshi, C.; Kubota, Y.; Kuroiwa, Y.; Sugimoto, K. High-Throughput Powder Diffraction Measurement System Consisting of Multiple MYTHEN Detectors at Beamline BL02B2 of SPring-8. *Rev. Sci. Instrum.* **2017**, *88* (8), 085111.
(76) Kawaguchi, S.; Takemoto, M.; Tanaka, H.; Hiraide, S.; Sugimoto, K.; Kubota, Y. Fast Continuous Measurement of Synchrotron Powder Diffraction Synchronized with Controlling Gas and Vapour Pressures at Beamline BL02B2 of SPring-8. *J. Synchrotron Radiat.* **2020**, *27* (3), 616−624.
(77) Hattne, J.; Martynowycz, M. W.; Penczek, P. A.; Gonen, T. MicroED with the Falcon III Direct Electron Detector. *IUCrJ.* **2019**, *6* (5), 921−926.
(78) Kabsch, W. XDS. *Acta Crystallogr. D Biol. Crystallogr.* **2010**, *66* (2), 125−132.
(79) Sheldrick, G. M. *SHELXT* − Integrated Space-Group and Crystal-Structure Determination. *Acta Crystallogr. Sect. Found. Adv.* **2015**, *71* (1), 3−8.
(80) Emsley, P.; Lohkamp, B.; Scott, W. G.; Cowtan, K. Features and Development of *Coot*. *Acta Crystallogr. D Biol. Crystallogr.* **2010**, *66* (4), 486−501.
(81) Ercius, P. *DuSC_explorer, Ver. 1 0.* https://github.com/ercius/DuSC_explorer
(82) Savitzky, B. H.; Zeltmann, S. E.; Hughes, L. A.; Brown, H. G.; Zhao, S.; Pelz, P. M.; Pekin, T. C.; Barnard, E. S.; Donohue, J.; Rangel DaCosta, L.; Kennedy, E.; Xie, Y.; Janish, M. T.; Schneider, M. M.; Herring, P.; Gopal, C.; Anapolsky, A.; Dhall, R.; Bustillo, K. C.; Ercius, P.; Scott, M. C.; Ciston, J.; Minor, A. M.; Ophus, C. py4DSTEM: A Software Package for Four-Dimensional Scanning Transmission Electron Microscopy Data Analysis. *Microsc. Microanal.* **2021**, *27* (4), 712−743.

https://doi.org/10.1021/jacs.5c19737
J. Am. Chem. Soc. 2026, 148, 8474−8486